9-2014

Reduced Diaphyseal Strength Associated with High Intracortical Vascular Porosity within Long Bones of Children with Osteogenesis Imperfecta

Carolyne Albert
Marquette University, carolyne.albert@marquette.edu

John Jameson
Marquette University, john.jameson@marquette.edu

Peter Smith
Rush University

Gerald F. Harris
Marquette University, gerald.harris@marquette.edu

Reduced Diaphyseal Strength Associated with High Intracortical Vascular Porosity Within Long Bones of Children with Osteogenesis Imperfecta

Carolyne Albert
Shriners Hospitals for Children-Chicago, Chicago, IL
Department of Biomedical Engineering, Marquette University, Orthopaedic and Rehabilitation Engineering Center (OREC), Milwaukee, WI

John Jameson
Advanced Light Source, Lawrence Berkeley National Laboratory, Berkeley, CA
Department of Biomedical Engineering, Marquette University, Orthopaedic and Rehabilitation Engineering Center (OREC), Milwaukee, WI

Peter Smith
Shriners Hospitals for Children-Chicago, Chicago, IL
Department of Orthopedic Surgery, Rush University Medical Center, Chicago, IL

Gerald Harris
Shriners Hospitals for Children-Chicago, Chicago, IL
Department of Biomedical Engineering, Marquette University, Orthopaedic and Rehabilitation Engineering Center (OREC), Milwaukee, WI

Abstract

Osteogenesis imperfecta is a genetic disorder resulting in bone fragility. The mechanisms behind this fragility are not well understood. In addition to characteristic bone mass deficiencies, research suggests that bone material properties are compromised in individuals with this disorder. However, little data exists regarding bone properties beyond the microstructural scale in individuals with this disorder.

Specimens were obtained from long bone diaphyses of nine children with osteogenesis imperfecta during routine osteotomy procedures. Small rectangular beams, oriented longitudinally and transversely to the diaphyseal axis, were machined from these specimens and elastic modulus, yield strength, and maximum strength were measured in three-point bending. Intracortical vascular porosity, bone volume fraction, osteocyte lacuna density, and volumetric tissue mineral density were determined by synchrotron micro-computed tomography, and relationships among these mechanical properties and structural parameters were explored.

Modulus and strength were on average 64–68% lower in the transverse vs. longitudinal beams ($P < 0.001$, linear mixed model). Vascular porosity ranged between 3 and 42% of total bone volume. Longitudinal properties were associated negatively with porosity ($P \leq 0.006$, linear regressions). Mechanical properties, however, were not associated with osteocyte lacuna density or volumetric tissue mineral density ($P \geq 0.167$). Bone properties and structural parameters were not associated significantly with donor age ($P \geq 0.225$, linear mixed models).

This study presents novel data regarding bone material strength in children with osteogenesis imperfecta. Results confirm that these properties are anisotropic. Elevated vascular porosity was observed in most specimens, and this parameter was associated with reduced bone material strength. These results offer insight toward understanding bone fragility and the role of intracortical porosity on the strength of bone tissue in children with osteogenesis imperfecta.

Keywords

Osteogenesis imperfecta, Pediatric bone, Flexural properties, Strength, Intracortical porosity

1. Introduction

Osteogenesis imperfecta (OI), also known as brittle bone disease, is a genetic disorder related to type I collagen and resulting in a high susceptibility to bone fractures [1]. The true prevalence of OI is unknown; however, it has been estimated to affect between 1:30,000 and 1:5000 births [1], [2], [3], [4]. There is no cure for OI. Severity varies widely, from mild to lethal in the perinatal period, and several genetic mutations have been associated with various types of OI [5], [6], [7], [8]. The mechanisms responsible for bone fragility in OI, however, remain poorly understood, and better understanding of these mechanisms is of high value toward identifying new treatment and rehabilitative strategies for individuals with this disorder.

Bone fragility in OI likely stems in part from a characteristic low bone mass. Individuals with OI tend to have very low areal bone mineral density (aBMD), which can be the result of decreased bone size and/or decreased volumetric bone mineral density (vBMD) [9], [10]. In a backscattered electron imaging study of iliac crest biopsies, cortical and trabecular bone were described as “markedly sparse” in children with severe and

moderately severe forms of OI, and a “dearth of bone” was noted in some children with mild OI [11]. Decreased trabecular and cortical thickness, as well as reduced bone volume fraction were also observed in histomorphometric studies of iliac crest biopsies from children with OI [12], [13].

In addition to bone mass deficiencies, several abnormalities in bone tissue composition have been described, and these irregularities may also contribute to the characteristic bone fragility. The causative genetic defects in OI are related to type I collagen, the main organic component of bone. A mild form of the disorder, OI type I, has been attributed to an insufficient production of type I collagen [14], [15], [16], [17]. More severe forms, OI types III and IV, have been linked to amino substitution defects within the collagen molecules [6], [17], [18], while recently identified recessive forms of the disorder have been associated with deficiencies in other proteins that interact with collagen [5], [19]. Irregularities in collagen fibril diameters have also been observed in the OI population [20], [21], [22]. Within the inorganic matrix, alterations in the size, shape, and composition of the bone mineral crystals [20], [23], [24], and increased matrix mineralization density have been noted in children with OI [13], [25], [26]. Murine models have provided support to the hypothesis that the brittleness of bone in OI can be attributed in part to compromised material properties of the bone tissue. For example, in mouse models of mild and severe forms of OI (*mov13* and *oim* models, respectively) bone material strength was 11–43% lower than that of control mice [27], [28], [29]. It has not been confirmed, however, whether these observations are also true in humans, as little data is yet available to describe bone material strength in individuals with this condition [30].

A few previous studies have used nanoindentation to measure elastic modulus, a property denoting material-level stiffness, for pediatric OI bone [25], [31], [32], [33], [34]. Within that microstructural scale, the elastic modulus of bone tissue was found to be higher in children with severe or moderately severe OI (types III and IV) vs. age-matched controls [25], and this property was slightly higher in children with mild (type I) vs. severe (type III) OI [31]. Interestingly, contrary to observations in normal bone tissue [35], [36], [37], no significant difference in modulus was observed between indents taken parallel vs. perpendicular to the long bone axis [32], which led to the speculation that OI bone may exhibit more isotropic properties than does typical bone. These results confirm that bone material properties are affected in OI; however, important limitations with these studies should be acknowledged. First, the small size of the indents excluded the effects of pores such as vascular spaces, which can largely influence the “effective” material properties at the mesoscale. Therefore, due to the complex hierarchical structure of bone, it is not clear whether these observations made within the microstructural scale hold true in OI bone at larger scales. Finally, these nanoindentation studies do not provide any information regarding bone material strength, an important property in determining fracture risk.

In a recent pilot study by our group, two osteotomy specimens from long bone diaphyses of children with OI were tested in bending [30], and their bone material strength was lower than values reported for typical pediatric bone [38]. Visual inspection of these bone specimens revealed the appearance of considerable porosity within a tissue region that is typically occupied by dense cortical bone: throughout the mid-diaphyseal cortex, near to the periosteal surface. Based upon this observation, it was speculated that the decreased strength observed in those bone specimens could be the result of abnormally high intracortical bone porosity. Further investigation by high-resolution computed tomography confirmed the presence of unusually high vascular porosity, on average 21%, within long bone diaphyseal cortex of children with OI, when compared with control specimens from children with no known musculoskeletal disease, for which the average porosity was 3% [39]. A similar finding was since then reported by another group in a scanning electron microscopy study of mid-diaphyseal osteotomy specimens from children with OI type III, which described the presence of “flattened and elongated lacunar spaces” within regions of bone “normally taken up by compact cortex” [40]. The current study builds upon our group's recent work, and offers an in-depth analysis of relationships between cortical tissue architecture, including vascular porosity, and the mechanical properties of diaphyseal bone in children with OI.

The specific objectives of this study were as follows: (1) to measure the flexural properties, i.e., elastic modulus, flexural yield strength, and maximum flexural strength, of cortical bone tissue from the long bone diaphyses of children with OI; (2) to assess anisotropy within OI bone tissue by comparing the material properties of specimens oriented transversely vs. longitudinally to the long bone axis; and (3) to explore relationships between the material properties and intracortical vascular porosity in this population. Relationships between the mechanical properties and other microstructural parameters, namely osteocyte lacuna density and volumetric tissue mineral density, were also explored.

2. Materials and methods

2.1. Bone specimens

Twelve cortical bone specimens were collected from long bone diaphyses of nine children with OI (Table 1, Table 2). These specimens, varying in shapes and sizes, were obtained during routine corrective orthopaedic surgeries (Table 2) at Shriners Hospitals–Chicago, with informed consent/assent from the donors and under an IRB-approved protocol (Rush University Medical Center #10101309, Marquette University #HR-2167).

Table 1. Donor details: clinical severity and OI type, gender, age at time of specimen donation, and history of bisphosphonate therapy administered prior to specimen donation.

Donor	Disease severity	Clinical OI type[a]	Gender	Specimen	Age	Bisphosphonate therapy prior to specimen donation
1	Mild	I (I)	F	1	6	Pamidronate, several treatments
2	Mild	I	F	2	11	Pamidronate, one course of treatment
3	Moderately severe	IV (III–IV)	M	3[b]	9	None
				4[b]	11	Pamidronate, two courses of treatment
4	Moderately severe	IV (IV)	F	5	8	Pamidronate, one course of treatment
5	Moderately severe	III	M	6[c]	14	Pamidronate, several treatments
				7[c]	14	Pamidronate, several treatments
6	Severe	III	F	8[d]	3	Pamidronate, several treatments
				9[d]	3	Pamidronate, several treatments
7	Severe	III	F	10	6	Pamidronate, one course of treatment
8	Severe	III	F	11	9	None
9	Severe	III (VIII)	M	12	16	Alendronate, three years of treatment

aOI type is based on the Sillence classification [8]. Genotype, if known, is indicated in parentheses.
bSpecimens 3 and 4 were obtained from contralateral tibiae of donor 3 within a 2-year interval. The donor had not been treated with bisphosphonates prior to donating specimen 3, but had received two 3-day courses of pamidronate prior to donating specimen 4.
cSpecimens 6 and 7 were obtained simultaneously from the contralateral tibiae of donor 5 during an elective surgical procedure.
dSpecimens 8 and 9 were obtained simultaneously from the contralateral femora of donor 6 during an elective surgical procedure.

Table 2. Specimen descriptions: harvest site, surgical procedure during which the specimen was harvested, presence or absence of a recent fracture at or near the osteotomy site, and number of beams tested in bending

from each osteotomy specimen that were oriented longitudinally (L) and transversely (T) to the long bone axis (in parentheses is the number of beams imaged by micro-computed tomography).

Donor	Specimen	Harvest site	Surgical procedure	Recent fracture at site?	Beams tested in bending (imaged)	
					L	T
1	1	Tibia, mid-diaphysis	Fracture repair, rod revision	Yes	6 (1)	2 (0)
2	2	Femur, mid-diaphysis	Fracture repair, rod revision	Yes	3 (2)	0 (0)
3	3[a]	Tibia, mid-diaphysis	Rodding for fracture non-union	Yes	3 (1)	1 (1)
	4[a]	Tibia, mid-diaphysis	Deformity correction, rod revision	No	3 (1)	1 (1)
4	5	Humerus, proximal diaphysis	Deformity correction, rod revision	Yes (healed)	9 (1)	3 (1)
5	6[b]	Tibia, mid-diaphysis	Rod revision, elective	No	2 (1)	1 (1)
	7[b]	Tibia, mid-diaphysis	Rod revision, elective	No	0 (0)	1 (1)
6	8[c]	Femur, mid-diaphysis	Corrective rodding	No	4 (1)	2 (1)
	9[c]	Femur, mid-diaphysis	Corrective rodding	No	3 (1)	2 (1)
7	10	Tibia, proximal diaphysis	Rod revision due to pain	No	0 (0)	2 (1)
8	11	Tibia, mid-diaphysis	Rod revision, elective	No	1 (1)	1 (1)
9	12	Tibia, mid-diaphysis	Corrective rodding	No	6 (1)	3 (1)

aSpecimens 3 and 4 were obtained from contralateral tibiae of donor 3 within a 2-year interval.
bSpecimens 6 and 7 were obtained simultaneously from the contralateral tibiae of donor 5 during an elective procedure to revise intramedullary rods.
cSpecimens 8 and 9 were obtained simultaneously from the contralateral femora of donor 6 during an elective procedure to correct deformity of the femoral diaphyses.

2.2. Specimen preparation

The bone specimens were machined into a total of 59 rectangular beams with a low speed diamond saw (IsoMet Low Speed Saw, Buehler, Lake Bluff, IL) and a 0.3 mm-thick wafering blade (Series 15HC Diamond, Buehler, Lake Bluff, IL), using methods described and validated in earlier work [30]. Beam dimensions of approximately 5–6 mm in length, 0.7 mm in depth, and 1 mm in width were chosen based on the dimensions of the smallest of these donated osteotomy specimens. Each specimen was kept fresh-frozen at − 85 °C prior to machining and testing. Machining of the beams was achieved with the following steps. Under constant irrigation, each specimen was first machined into a slice having a thickness equal to the desired beam depth. These specimens were small and varied in size and shape; however, care was taken to obtain the beams from a relatively

consistent location. The beams were cut from a slice of bone that was obtained as close as possible to the periosteal surface. This was achieved by gluing the periosteal surface onto a wood mandrel and making two consecutive cuts at distances of 1.2 and 0.2 mm, respectively, from the referenced periosteum–mandrel interface. These cut distances were selected taking into account the thickness of the wafering blade. The slice was subsequently cut into beams of the desired width. While cutting each slice into beams, the slice was gripped onto a ¼-inch thick acrylic backing to prevent undue bending deformation of the slice. Each beam was machined such that its long axis was oriented either longitudinally (i.e., proximal–distal orientation, 40 beams) or transversely (i.e., circumferential direction, 19 beams) relative to the long bone axis of the donated specimen (Table 2). Beam depth and width were measured with a digital micrometer (Model 293–340, Mitutoyo Corporation, Japan), and the average depth and width were 668 μm (standard deviation 60 μm) and 1005 μm (46 μm), respectively.

2.3. Flexural testing

Each beam was loaded to failure using a three-point bending test assembly designed for the specific purpose of characterizing small bone specimens [30]. The loading nose and supports consisted of 1/16-in. (1.59 mm) diameter stainless steel dowel pins, which were fixed into grooves machined in an upper and a lower aluminum platen using cyanoacrylate. A span length (L) of 4 mm (actual measurement 3.973 mm) was chosen to accommodate the size of the osteotomy specimens that were collected for this study. The bending jig was assembled onto an electromechanical testing system (Model 3345, Instron®, Norwood, MA, USA) with a 50 N capacity load cell (Model 2519–102, Instron®, Norwood, MA, USA). An external linear variable differential transformer, LVDT (Model 2601, Instron®, Norwood, MA, USA), was used to determine beam deflection at the mid-span.

Flexural loading was controlled using Bluehill 2 Software (Instron®, Norwood, MA). Each test consisted of five cycles of preconditioning (0.05–1.0 N for longitudinal beams, and 0.05–0.5 N for transverse beams) with a crosshead displacement rate of 0.2 mm/min, followed by a ramp to failure at a constant deflection rate (as measured by the LVDT) of 2.0 mm/min. This deflection rate resulted in a tensile surface strain rate of approximately 0.009 s^{-1} at the mid-span. Load and beam deflection data were collected at a sampling rate of 100 Hz throughout the test series. Each beam specimen was kept hydrated in normal saline until testing and was maintained hydrated during the test, which had a duration of approximately 2 min, using a drop of saline that remained in place on the tension side of the beam by surface tension.

Flexural stress and flexural strain were calculated from the load and deflection data using the following equations based on linear elastic beam theory [41]:σf=3FL2wd2andεf=6dδL2where w is the specimen width; d is the specimen depth; L is the span length; F is the load; δ is the beam deflection at mid-span, i.e., displacement measured by the LVDT; and σ_f and ε_f are the calculated stress and strain at the tensile surface at mid-span, respectively.

The following properties were calculated from the flexural stress–strain data obtained during the ramp to failure using a custom Matlab script (R2012a, Mathworks, Natick, MA, USA). Maximum flexural strength ($\sigma_{f,max}$) was defined as the maximum calculated flexural stress before failure. Elastic modulus (E) and flexural yield strength ($\sigma_{f,y}$) were determined using the following iterative process. An initial estimate of the modulus was calculated as the slope between two arbitrary points that were selected within the linear region of the flexural stress–strain curve. An initial estimate of yield strength was calculated using this modulus value and the 0.2% strain offset method. A new estimate of elastic modulus was then calculated as the slope between one and two thirds of the previous yield strength estimate, and the new modulus was used to calculate a new yield strength value using the same offset method. The latter process was repeated until convergence of the modulus and yield strength results, which occurred within 10 iterations.

2.4. Micro-computed tomography

Following mechanical testing, 21 beams (Table 2) were imaged by synchrotron micro-computed tomography, SR-μCT (Beamline 8.3.2, Advanced Light Source, Lawrence Berkeley National Laboratory, Berkeley, CA), and the following microstructural parameters were determined: vascular porosity, volumetric tissue mineral density, and osteocyte lacunar density. Each beam was air-dried overnight and mounted upright onto a sample holder using capillary sealing wax and a wax pen. The sample holder was then gripped via a drill chuck assembly attached to a standard optical kinematic mount, which in turn was mounted onto a magnetically coupled rotational stage. To minimize phase contrast effects, a newly commissioned X-ray microscope (Optique Peter, Lentilly, France), described in previous work [42], was used allowing a minimum sample-to-scintillator distance of 7 mm. For each scan, a total of 1025 projections were collected over a continuous 180° rotation at a monochromatic X-ray energy of 17 keV. After passing through the sample, attenuated X-rays were converted into visible light via a thin, single-crystal scintillator, magnified via objective optics, and imaged onto the camera (pco.edge sCMOS camera, PCO-TECH Inc, Romulus, MI). This camera/optics setup yielded a horizontal field of view of 1.7 mm and an imaged pixel size of 0.65 μm.

Tomographic reconstructions were performed using Octopus 8.6 software (inCT, Ghent, Belgium), with resulting 16-bit grayscale data sets consisting of 2160 slices each having 2000 × 2000 pixels. For each beam, vascular porosity calculations were carried out within a 0.6 mm^3 rectangular prismatic region of interest (ROI). Visual inspection of the SR-μCT scans revealed that microdamage was present within a region extending approximately 0.25 mm on either side of the fracture induced during the mechanical test. The ROI from which the microstructural parameters were calculated for each beam was located at least 0.5 mm away from the fracture site, thus excluding the fracture and associated local microdamage from the bending test.

Each scan was segmented into its microstructural elements (i.e., bone, vascular porosity, and osteocyte lacunae) following previously described masking procedures [43], [44]. The high contrast and spatial resolution of the SR-μCT images produced clear bimodal histograms. Thus, an initial bone mask was generated by blurring each dataset with a simple Gaussian low-pass filter (to remove all osteocyte lacunae) and thresholding with the built-in iterative IsoData algorithm on the stack histogram. A lacunar mask was then created from within the bone mask by (1) thresholding the original image stack, (2) inverting the result, and (3) performing the logical “AND” operation with the bone mask. Finally, a vascular porosity mask was produced through inversion of the bone mask. Subsequent quantitative analysis of the binary vascular and lacunar porosity masks was performed using ImageJ [45] and the plug-in BoneJ [46].

Intracortical vascular porosity, defined as the relative volume occupied by Haversian canals, Volkmann canals, and resorption spaces [47], was determined from the vascular porosity mask within the ROI for each scanned beam. Prior to this calculation, a connected-components algorithm in BoneJ was used to label individual pores. Virtual despeckling was performed to remove all pores smaller than 2000 μm^3, as these have previously been shown to represent noise and other spuriously segmented particles such as ring artifacts and small microdamage (if present) [44], [48], [49], [50]. Vascular porosity was then determined from the volume ratio of all remaining vascular voxels. Cortical bone volume fraction (V_f) was calculated as “1 − vascular porosity.” Three-dimensional visualizations of the bone and intracortical porosity spaces were generated with Avizo 7.1 software (Visualization Sciences Group, FEI, Mérignac, France).

Osteocyte lacunae were labeled and counted from the lacunar mask by connected-components analysis in accordance with a previously validated segmentation rule [44]. Initial denoising was performed by removing all particles smaller than 82 μm^3 as well as those larger than 2000 μm^3 [44], [48], [49], [50]. Restrictions were then invoked on two shape-based osteocyte lacunar descriptors that were automatically calculated as part of the labeling routine, namely the particle Euler number (χ) and the major/intermediate axis anisotropy ratio. The

Euler number is a topological property commonly used in connectivity analysis [51], [52]. Any solid body that can be rigidly deformed into a sphere has a χ of one. Thus any particle whose χ was not one was removed. Moreover, since highly prolate (i.e., rod-like) spheroids are commonly associated with ring artifacts, any particle whose major/intermediate axis anisotropy ratio was greater than five was removed. To avoid biasing of the results from truncated lacunae, any particle in contact with the one of the six edges in the image stack volume was eliminated. Osteocyte lacunar density was then calculated as the number of lacunae in the ROI tissue volume.

In SR-μCT, the X-ray photon energy is truly monochromatic and the linear attenuation values determined during the reconstruction process are directly proportional to the degree of mineralization [53]. Calculation of volumetric tissue mineral density was thus carried out by segmenting out all non-bone voxels from the original image using a histogram-based threshold [54], and then determining the mean linear attenuation coefficient of the remaining bone voxels ($\mu_{b,avg}$). The X-ray mass attenuation of bone, or $(\mu/\rho)_b$, is an energy-dependent material property that can be determined from tabulated values in the National Institute of Standards and Technology database [55]. Volumetric tissue mineral density was calculated from the ratio $\mu_{b,avg}$ divided by $(\mu/\rho)_b$. The X-ray photon energy was calibrated prior to bone imaging using thin metallic foils (silver and germanium) having known X-ray attenuation properties [56].

2.5. Statistical analysis

To assess whether the material properties are anisotropic in these bone specimens, the measured flexural properties were compared between the longitudinal and transverse beams using linear mixed model analysis with random specimen effect. Simple linear regression analysis was used to explore linear relationships among mechanical properties and microstructural parameters for each group of beams, i.e., longitudinal and transverse, and test for their statistical significance. Power law relationships were explored between each property and the bone volume fraction, as such relationships have been observed in normal bone tissue [57], [58], [59], [60], [61], [62]. Finally, linear mixed models were used to investigate relationships between donor age and the mechanical properties and structural parameters.

3. Results

3.1. Three-point bending

Representative flexural load–displacement curves for each specimen orientation are presented in Fig. 1. The mechanical properties differed significantly ($P < 0.001$, linear mixed model) between the longitudinal and transverse beams: on average, modulus, yield strength, and maximum strength were 64–68% lower for the transverse beams than for the longitudinal ones (Table 3). The mechanical properties did not vary significantly with donor age (Table 4).

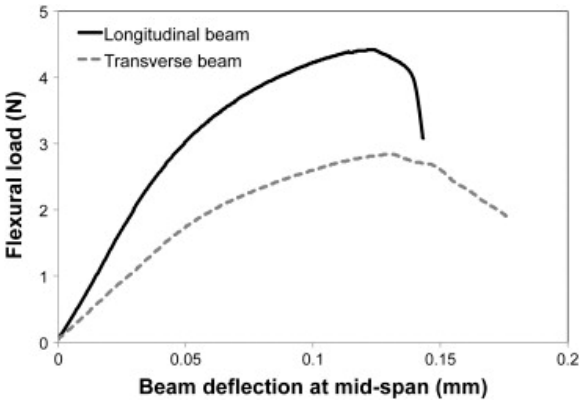

Fig. 1. Flexural load–displacement curves for beams of bone oriented longitudinally (black) and transversely (gray) to the long bone axis. These beams were obtained from the humeral diaphysis of an 8 year-old female donor with OI type IV (specimen 5).

Table 3. Flexural properties of pediatric OI bone specimens oriented longitudinally and transversely to the diaphyseal axis: elastic modulus (E), yield strength ($\sigma_{f,y}$), and maximum strength ($\sigma_{f,max}$). Average (standard error), based on linear mixed model analysis.

Orientation	***E* (GPa)**	**$\sigma_{f,y}$ (MPa)**	**$\sigma_{f,max}$ (MPa)**
Longitudinal	4.4 (0.4)	61.4 (5.3)	83.0 (7.8)
Transverse	1.6 (0.4)∗	20.8 (6.0)∗	26.5 (8.6)∗

∗$P < 0.001$ between longitudinal and transverse properties.

Table 4. Relationships between bone material properties and donor age (in years), based on linear mixed model analysis with specimen number as a random effect factor. Average (standard error).

Material property	**Intercept**	**Slope**	***P* value for slope**
Longitudinal			
Elastic modulus (GPa)	5.54 (1.34)	− 0.11 (0.14)	0.430
Yield strength (MPa)	77.17 (18.13)	− 1.46 (1.83)	0.433
Maximum strength (MPa)	103.79 (27.65)	− 1.81 (2.78)	0.545
Transverse			
Elastic modulus (GPa)	1.44 (0.71)	0.00 (0.07)	1.000
Yield strength (MPa)	15.33 (8.40)	0.27 (0.85)	0.767
Maximum strength (MPa)	18.50 (10.35)	0.29 (1.04)	0.828

3.2. Micro-computed tomography results

Intracortical vascular porosity varied between 3% and 42% (average 21%, standard deviation 10%), and, consequently, volume fraction averaged 0.79 (standard deviation 0.10). These measures did not differ significantly between the longitudinal and transverse beam specimens, as expected. The average vascular porosity was 21% (standard error 3%) for the longitudinal beams vs. 22% (3%) for the transverse ones ($P = 0.731$, linear mixed model). Fig. 2 illustrates three-dimensional visualizations of the ROIs within longitudinal and transverse beams from specimen 9 (femur mid-diaphysis from a 3 year old female with OI type III). Visual inspection of the scans confirmed that the predominant orientation of vascular pores was parallel to the beam axis for longitudinal beams and perpendicular to the beam axis for the transverse ones (Fig. 2, bottom). Average osteocyte lacunar density was 35661 mm^{-3} (standard deviation 13118 mm^{-3}). Mean volumetric tissue mineral density was 1.63 g/cm^3 (standard deviation 0.14 g/cm^3). Finally, vascular porosity, osteocyte lacunar density, and volumetric tissue mineral density were not significantly associated with donor age (Table 5).

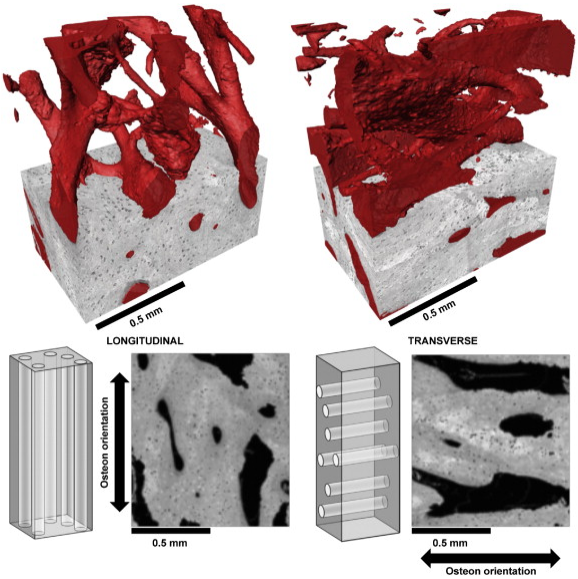

Fig. 2. Three-dimensional tomographic assessment of OI cortical bone structure. SR-μCT images of OI bone show vascular porosity in longitudinal (top, left; vascular porosity = 16%) and transverse (top, right; vascular porosity = 21%) beams from the femoral mid-diaphysis of a 3 year-old female (donor 6) with OI type III. Idealized drawings of longitudinal (bottom, left) and transverse (bottom, right) beams, along with corresponding tomographic slices, illustrate the predominant orientation of osteons in each beam. Although both orientations displayed a similarly high degree of vascular porosity (16% for the longitudinal beam and 21% for the transverse one), the longitudinally oriented beam had much higher strength than did the transverse one (maximum flexural strength were 78 vs. 15 MPa, respectively).

Table 5. Relationships between microstructural parameters and donor age (in years) based on linear mixed model analysis. Average (standard error).

Microstructural parameter	**Intercept**	**Slope**	***P* value for slope**
Vascular porosity (%)	23.97 (8.09)	− 0.25 (0.80)	1.000
Osteocyte lacunar density (mm^{-3})	44971 (9265)	− 1060 (912)	0.225
Volumetric tissue mineral density (g/cm^3)	1.67 (0.09)	− 0.00 (0.01)	0.665

3.3. Relationships among mechanical properties and the microstructural parameters

For both beam orientations, positive linear relationships were observed between elastic modulus and each strength measure (Table 6). Highly significant ($P \leq 0.004$) negative correlations were found between vascular porosity and the longitudinal material properties (Table 6 and Fig. 3). Negative correlations were also observed between the transverse flexural properties and porosity; however, those correlations were not statistically significant ($P > 0.100$). The bone material properties were not associated significantly with osteocyte lacunar density ($P \geq 0.220$) or volumetric tissue mineral density ($P \geq 0.167$) (Table 6). Power law relationships between each longitudinal property and bone volume fraction are presented in Table 7.

Table 6. Pearson's correlation coefficients (*R*) and slopes for the linear regressions among the mechanical properties and microstructural parameters.

Bone material property	**Factor**	**Slope**	***R***	***P*-value**
Longitudinal				
Elastic modulus (GPa)	Vascular porosity (%)	**− 0.15**	**− 0.86**	**< 0.001**
	Osteocyte lacunar density (mm^{-3})	6.21 E − 5	0.40	0.220

	Volumetric tissue mineral density (g/cm^3)	4.98	0.35	0.285
Yield strength (MPa)	Elastic modulus (GPa)	**13.28**	**0.95**	**< 0.001**
	Vascular porosity (%)	**− 1.90**	**− 0.78**	**0.003**
	Osteocyte lacunar density (mm^{-3})	6.37 E − 4	0.30	0.377
	Volumetric tissue mineral density (g/cm^3)	49.9	0.25	0.450
Maximum strength (MPa)	Elastic modulus (MPa)	**17.47**	**0.90**	**< 0.001**
	Yield strength (MPa)	**1.34**	**0.97**	**< 0.001**
	Vascular porosity (%)	**− 2.58**	**− 0.77**	**0.004**
	Osteocyte lacunar density (mm^{-3})	4.92 E − 4	0.16	0.629
	Volumetric tissue mineral density (g/cm^3)	11.0	0.04	0.905
Transverse				
Elastic modulus (GPa)	Vascular porosity (%)	− 0.06	− 0.53	0.110
	Osteocyte lacunar density (mm^{-3})	2.92 E − 5	0.38	0.276
	Volumetric tissue mineral density (g/cm^3)	3.68	0.47	0.167
Yield strength (MPa)	Elastic modulus (MPa)	**9.29**	**0.91**	**< 0.001**
	Vascular porosity (%)	− 0.59	− 0.51	0.126
	Osteocyte lacunar density (mm^{-3})	4.83 E − 5	0.06	0.864
	Volumetric tissue mineral density (g/cm^3)	16.9	0.21	0.551
Maximum strength (MPa)	Elastic modulus (MPa)	**11.00**	**0.86**	**0.001**
	Yield strength (MPa)	**1.24**	**0.99**	**< 0.001**
	Vascular porosity (%)	− 0.68	− 0.47	0.166
	Osteocyte lacunar density (mm^{-3})	− 4.51 E − 6	0.00	0.990
	Volumetric tissue mineral density (g/cm^3)	14.4	0.15	0.687

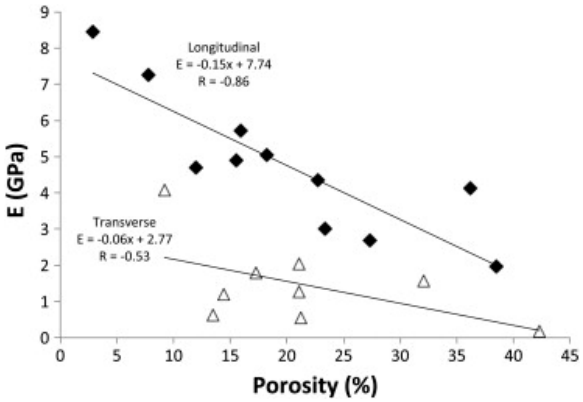

Fig. 3. Linear relationships between elastic modulus (*E*) and intracortical vascular porosity for OI bone oriented longitudinally (black diamonds) and transversely (white triangles) to the long diaphyseal axis.

Table 7. Power law relationships between longitudinal mechanical properties and bone volume fraction V_f (property = $a\ V_f^b$).

Mechanical property	**Relationship**	***a***	***b***	R^2
Elastic modulus (*E*, GPa)	$E = a\ V_f^b$	8.67	2.93	0.80
Yield strength ($\sigma_{f,y}$, MPa)	$\sigma_{f,y} = a\ V_f^b$	117.4	2.76	0.68
Maximum strength ($\sigma_{f,max}$, MPa)	$\sigma_{f,max} = a\ V_f^b$	162.1	2.83	0.66

4. Discussion

This study presents data from rare osteotomy specimens that were obtained during corrective surgeries in children with OI. Building upon previous efforts [30], [39], this study presents the first dataset describing the material strength of bone tissue in children with OI. The current results demonstrate that, similar to normal bone, OI bone exhibits anisotropic material behavior. SR-μCT imaging further revealed abnormally high vascular porosity within regions typically occupied by dense cortical bone, and this porosity was shown to be associated with a decrease in bone material strength and elastic modulus in these specimens.

Elastic modulus results from this study (Table 3 and Fig. 3) were lower than values measured by nanoindentation for pediatric OI bone, i.e., 13–24 GPa in the longitudinal direction [25], [31], [32], [33], [34]. This observation is not surprising, considering that nanoindentation tests are performed at a much smaller scale, within lamellar bone regions and excluding the effects of void spaces such as Haversian canals and resorption cavities. Furthermore, specimens in the current study were fresh-frozen and untreated, whereas those in the nanoindentation studies were dehydrated, a process that has been shown to increase modulus results [63], [64], [65]. Unlike previous data from a nanoindentation study, which suggested that OI bone may exhibit more isotropic properties than normal tissue [32], results from the current study demonstrated clear anisotropy in bone material properties at the mesoscale within this population, with the transverse properties being approximately equal to one third of their longitudinal counterparts. These observations indicate that the preferential orientation of the vascular porosity network is likely to play an important role in the anisotropic behavior of OI bone at the mesoscale. Longitudinal modulus results were also below tensile values reported previously for normal pediatric bone, i.e., 14–32 GPa [66].

Strong, linear relationships were observed between the strength measures and elastic modulus. This observation is similar to a previous finding in a study of bone from several species [67]. To the authors' knowledge, no other study has characterized bone tissue strength in individuals with OI; however, current maximum flexural strength results for OI bone (Table 3) were lower than values reported for normal bone tissue from children of an equivalent age group, i.e., 150–207 MPa [68]. The reduced modulus and strength obtained for the OI bone specimens are likely related to the substantial vascular porosity observed in these specimens.

Three-point bending tests are a common tool in characterizing the material properties of small bone specimens [27], [28], [29], [69], [70], [71], [72]. Bending configurations are often more practical than tensile tests, especially when specimen size is limited. Nonetheless, limitations that are inherent to bending tests should be acknowledged. First, bending moments are not uniform within the specimen. In three-point bending, the moment is maximum within the plane of the loading nose, i.e., at mid-span. Consequently, local tensile stresses are highest on the beam surface at mid-span, which is where fracture initiation is likely to occur. In tensile tests, on the other hand, stress distribution is more uniform, and fracture may initiate within regions of relative weakness, e.g., around pores or a crack. Furthermore, in bending tests, strains within the specimen are calculated using beam theory, which assumes that the material behaves linear elastically. In materials that exhibit post-yield deformation, such as bone, however, this assumption is not valid beyond the yield point. The result is an overestimation of ultimate strength compared with values obtained from a tensile test. A more in-depth discussion of this phenomenon can be found in previous works [73], [74]. It is also worth noting that a minimum span/depth ratio of eight has been recommended when measuring the bending properties of ceramic materials [75]. In bone, elastic modulus results from bending tests were found to decrease with decreasing span/depth ratio when this ratio is less than 15, while this property was more consistent with a ratio of 20 or higher [76]. In the current study, a span of 4 mm was chosen to accommodate the small size of the osteotomy specimens. With this span, beam depth of 500 or 250 μm would have been required for a span/depth ratio of 8 or 15, respectively. Elastic modulus results for bone were found to be fairly constant for beam depths greater than 500 μm; however, those values were found to decrease sharply for smaller beam depths [70]. A

span/depth ratio of 6 was chosen for this study (i.e., depth of approximately 650 μm) based upon a validation study in which this dimension resulted in appropriate modulus results for bovine bone and acrylic beams [30]. Care was taken to ensure relatively constant depth between the beams (average 668 μm, standard deviation 60 μm) to minimize any undue experimental variability caused by changes in this parameter. It should nevertheless be acknowledged that the relatively low span/depth ratio used in this study may have resulted in some error caused by undue shear deformation within the specimens [75], [76].

SR-μCT imaging revealed substantial and heterogeneous vascular porosity within these diaphyseal bone specimens, i.e., accounting for 3–42% of the total bone volume. In most specimens, this porosity was much higher than typical values for children and young adults, i.e., 3–6% [39], [77], [78]. It is unlikely that the high porosity observed was influenced by the presence of smaller pores or flaws within the bone microstructure, such as microdamage and osteocyte lacunae. As discussed earlier, porosity was measured away from the region of microdamage surrounding the test-induced fracture. Furthermore, with dimensions on the order of 1 μm in thickness and 100 μm in length/width, microcracks typically account for less than 0.5% of the total bone volume in cortical bone [79], [80], [81], [82]. Visual inspection of all ROIs confirmed the presence of high vascular porosity with no obvious microdamage. Recent μCT studies on fatigue microdamage accumulation in human bone have proposed the use of contrast agents to aid in microcrack visualization and segmentation [79], [83]. However, these staining techniques are non-specific and label all void spaces including vasculature, osteocyte lacunae, and resorption spaces in addition to microcracks. Moreover, by nature these agents affect the reconstructed linear attenuation values (i.e., gray values) of the μCT scans, which undermines the ability to accurately quantify mineralization parameters such as volumetric tissue mineral density. Finally, differentiation of prior in vivo microdamage from that induced by the mechanical test requires scanning the bone specimens before and after mechanical testing. However, a previous study at the ALS showed that the high radiation dose associated with the current beamline causes a rapid decrease in bone mechanical properties [84]. For the current study, an accepted masking procedure was used during segmentation to label all vascular pores [43], [44], and a lower size restriction of 2000 μm^3 was imposed to minimize the inclusion of any artifacts or spuriously labeled lacunae (which are typically smaller than 500 μm^3 in volume) [44], [48], [49], [50]. Low bone mass is a characteristic clinical feature of OI, and evidence of a discontinuous and porous cortical bone structure within the iliac crest and long bone diaphyses can be found in other reports [12], [13], [40], [43]. In a recent study, elevated cortex porosity observed within long bone diaphyses of children with OI was attributed to abnormal secondary remodeling, resulting in a combination of regular concentric osteons and large, flattened resorption spaces formed by drifting osteons [40].

In the current study, significant negative associations were observed between longitudinal bone material properties and porosity. Similar relationships have been reported for normal cortical bone tissue from the mid-femoral diaphysis [85]. It is worth noting that, for the two beam specimens having the lowest porosity, i.e., 3% and 8%, longitudinal maximum flexural strength results (176 and 145 MPa, respectively) were comparable to the values reported for normal pediatric bone, i.e., 150–207 MPa [68]. Power law relationships have been reported between bone properties (i.e., strength and modulus) and density measures in several studies of trabecular and cortical bone [57], [58], [59], [60], [61], [62]. These relationships have been presented in the form of property = $a \times \text{density}^b$, with the resulting exponent typically ranging between 2 and 3. For example, in a study of cortical bone from many species, longitudinal elastic modulus was observed to follow a power law relationship with bone volume fraction, V_f: modulus = $a \times V_f^3$ [57]. In the current study, longitudinal bone properties followed similar power law relationships with bone volume fraction, in which the exponent "*b*" was 2.8 for strength, and 2.9 for modulus. These observations indicate that high intracortical porosity (thus, low bone volume fraction) may be an important contributing factor to bone fragility in children and adolescents with OI. Large pores within the cortex are likely to act as stress-raisers [86], resulting in increased local stresses and causing fracture to occur at lower levels of nominal stress.

In contrast with the longitudinal properties, relationships between transverse properties and vascular porosity were not statistically significant. This observation is similar to a finding from a previous study, in which transverse tensile and shear moduli were not significantly correlated with cortical porosity in adult human bone from the femoral diaphysis [85]. In that study, the authors concluded that the transverse elastic properties of cortical bone appeared to be less sensitive to variations in porosity than were those in the longitudinal direction. It was further proposed that this difference may be related to a lack of relationship observed between transverse and longitudinal properties. Nonetheless, it is worth noting that some relationships between density and orthogonal elastic properties of bone have been reported in other studies [87], [88]. It is therefore possible that a larger sample size might have revealed more significant relationships between transverse OI bone properties and vascular porosity.

Although osteocyte lacunae have been described by some investigators as sites of localized stress/strain concentration [89], [90] and preferential sites for microdamage initiation [91], the osteocyte lacunar density was not significantly associated with the mechanical properties measured in the current study. In fact, while significant relationships were observed between OI bone mechanical properties and vascular porosity, these properties were not significantly associated with either of the two material-level microstructural parameters measured, i.e., volumetric tissue mineral density and osteocyte lacunar density. The absence of significant relationships between the bone properties and these material-level parameters indicates that at the mesoscale the effective material properties of cortical bone in OI are likely related primarily to the “amount” of bone material present rather than to the “quality” of the bone material itself.

A wide range of values has been reported for osteocyte lacunar density owing to a number of experimental factors including donor age, local anatomical sampling site, image resolution, and segmentation strategy [44], [49], [50], [92], [93], [94], [95]. For example, one study on diaphyseal femoral bone noted a significant decrease in osteocyte lacunar density for patients aged 16–73 who had no known history of bone disease [94]. However, a recent SR-μCT study on a similar donor age range observed no difference in lacunar density at the proximal femoral diaphysis [50]. Inter-study comparison of lacunar density is therefore difficult. Although we found no significant association between lacunar density and age in the current pediatric OI population, our results are within the range previously observed in young adult bone (e.g., 20,000–90,000 lacunae/mm^3) [49], [50], [95]. The role of osteocyte lacunar properties in bone adaptation and disease is still poorly understood. For example, Mullender et al. [96] found a decrease in areal lacunar density for osteoporotic females compared to adult controls, while a similar study by McCreadie et al. [48] found no significant difference in lacunar size or shape compared to controls. However, one recent SR-μCT study on the *oim* mouse model of severe OI noted a significant increase in lacunar density compared to wild-type littermates [43], which the authors attributed in part to the increased bone turnover seen in the disorder. In addition to inhibiting osteoclast activity, there is also recent evidence that bisphosphonates may reduce osteocyte cell death [97]. Future imaging studies including both OI and control human bone are warranted to determine treatment effects and differences in lacunar properties between healthy and diseased bone.

The specimens in this study were obtained from a relatively small and heterogeneous group of individuals, i.e., between 3 and 16 years of age and with clinical OI phenotypes ranging from mild to severe. These 12 specimens were obtained during intramedullary rodding procedures. Of these, four were obtained in the vicinity of a recent fracture site: specimens 1 and 2 were obtained during fracture repair procedures; specimen 3 near a site of fracture non-union; and specimen 5 near a healed fracture site. It is possible that accumulation of prior damage (microcracks) resulting from the clinical fractures remained present within those specimens at the time of testing, which may have compromised the mechanical properties. However, visual inspection confirmed that no apparent fracture or callus was present within these specimens. Furthermore, as discussed earlier, examination of the SR-μCT scans did not reveal microcracks to be present aside from those observed surrounding the

fracture induced by the mechanical test. These observations indicate that no significant microdamage was present prior to testing. Moreover, these four “fracture” specimens did not have the lowest properties observed in this study. In fact, the beams from specimen 3 had the highest longitudinal modulus (8.1 GPa on average), yield strength (119 MPa), and maximum strength (173 MPa) of all the specimens, while the beams from specimen 2 had the second highest yield and maximum strength values. Finally, although modulus and strength tend to increase with age in typical children and adolescent bones [68], no significant association was found between donor age and any of the mechanical properties or structural parameters measured in the current study. Nonetheless, further data is needed to explore heterogeneity in bone structure and properties in OI as a function of factors such as donor age, phenotype, and anatomic site.

Antiresorptive bisphosphonate therapies have become common in the treatment of OI, and these therapies are sometimes initiated during early childhood [98], [99]. These drugs have been beneficial in increasing bone mineral density and reducing the incidence of fragility fractures in individuals with osteoporosis [100], [101]. The long-term effects of bisphosphonates, particularly when treatment is initiated at a young age, however, are not yet well understood [102], [103]. There is concern, for example, that osteoclastic inhibition from these drugs and the associated decline in bone remodeling may have a detrimental effect on bone tissue quality [102], [104], [105], [106], [107]. In the current study, all specimens with the exception of two (specimens 3 and 11) were obtained from donors who had previously received bisphosphonate treatments. It may be worth noting that longitudinal strength was higher in one of the non-treated specimens, specimen 3 (average maximum flexural strength of three beams was 173 MPa), than in those from donors having undergone antiresorptive therapies (range 46–107 MPa); however, this was not the case for the other non-treated specimen (specimen 11, 80 MPa). Unfortunately, due to the limited number of non-treated specimens, it was not possible to assess reliably whether any statistically significant relationships exist between the bone material properties and prior bisphosphonate treatments. It is unlikely that bisphosphonate treatments were associated with the high vascular porosity observed in this study, as these antiresorptive drugs were, in fact, observed to reduce cortical porosity in postmenopausal and osteoporotic women [108], [109]. Nonetheless, bisphosphonates have been recently associated with increased risks of subtrochanteric, femoral shaft, and atypical femoral fracture [110], [111]. It is therefore possible that prior bisphosphonate therapies may have contributed to the reduced material strength observed in the current bone specimens; however, further research is needed to confirm this possible undesirable effect.

5. Conclusions

This study presents tissue-level characterization of cortical bone elastic modulus and strength in children and adolescents with OI. These bone material properties were found to be anisotropic and greater along the longitudinal diaphyseal axis than within the transverse plane. Intracortical vascular porosity was found to be elevated in these specimens, and the bone material properties were negatively correlated with this porosity. These observations indicate that bone fragility in OI may be attributed, at least in part, to an elevated presence of vascular pores within the diaphyseal cortex.

Acknowledgments

The authors wish to thank Kathy Reiners from Shriners Hospitals for Children – Chicago for coordinating the specimen collection. We extend our gratitude to Dr. Sergey Tarima, from the Medical College of Wisconsin Division of Biostatistics, for his help with the statistical analyses. We are also grateful for the assistance of beamline scientists Dr. Dula Parkinson and Dr. Alastair MacDowell from the Advanced Light Source (ALS) at the Lawrence Berkeley National Laboratory, in collecting the imaging data.

This work was supported by NIDRR grants H133P080005 and H133E100007 from the U.S. Department of Education, and grant UL1RR031973 from the Clinical and Translational Science Award (CTSA) program of the National Center for Research Resources (NRCC) and the National Center for Advancing Translational Science (NCATS). These contents, however, do not necessarily represent the policy of the Department of Education, and endorsement by the Federal Government should not be assumed. Finally, the study was also supported by research fellowships from Shriners Hospitals for Children as well as the ALS, a Division of the Lawrence Berkeley National Laboratory. The ALS is supported by the Director, Office of Science, Office of Basic Energy Sciences, of the U.S. Department of Energy under Contract No. DE-AC02-05CH11231.

References

[1] J.C. Marini. **Osteogenesis imperfecta: comprehensive management.** *Adv Pediatr*, 35 (1988), pp. 391-426

[2] P.H. Byers, R.D. Steiner. **Osteogenesis imperfecta.** *Annu Rev Med*, 43 (1992), pp. 269-282

[3] J.C. Marini. ***Chapter 692 Osteogenesis Imperfecta*, in *Nelson Textbook of Pediatrics.*** R.M. Kliegman, *et al.* (Eds.), Elsevier, Philadelphia, PA (2011)

[4] D.O. Sillence, K.K. Barlow. **Osteogenesis imperfecta, a handbook for medical practitioners and health care professionals.** *O. Society* (Ed.), Rydalmere, Australia (1992)

[5] A. Forlino, *et al.* **New perspectives on osteogenesis imperfecta.** *Nat Rev Endocrinol*, 7 (9) (2011), pp. 540-557

[6] J.C. Marini, *et al.* **Consortium for osteogenesis imperfecta mutations in the helical domain of type I collagen: regions rich in lethal mutations align with collagen binding sites for integrins and proteoglycans.** *Hum Mutat*, 28 (3) (2007), pp. 209-221

[7] M. Ben Amor, *et al.* **Osteogenesis imperfecta.** *Pediatr Endocrinol Rev*, 10 (Suppl. 2) (2013), pp. 397-405

[8] D.O. Sillence, A. Senn, D.M. Danks. **Genetic heterogeneity in osteogenesis imperfecta.** *J Med Genet*, 16 (2) (1979), pp. 101-116

[9] F. Rauch, B. Tutlewski, E. Schonau. **The bone behind a low areal bone mineral density: peripheral quantitative computed tomographic analysis in a woman with osteogenesis imperfecta.** *J Musculoskelet Neuronal Interact*, 2 (4) (2002), pp. 306-308

[10] F. Rauch, *et al.* **Bone mass, size, and density in children and adolescents with osteogenesis imperfecta: effect of intravenous pamidronate therapy.** *J Bone Miner Res*, 18 (4) (2003), pp. 610-614

[11] S.J. Jones, *et al.* **The microscopic structure of bone in normal children and patients with osteogenesis imperfecta: a survey using backscattered electron imaging.** *Calcif Tissue Int*, 64 (1) (1999), pp. 8-17

[12] F. Rauch, *et al.* **Static and dynamic bone histomorphometry in children with osteogenesis imperfecta.** *Bone*, 26 (6) (2000), pp. 581-589

[13] P. Roschger, *et al.* **Evidence that abnormal high bone mineralization in growing children with osteogenesis imperfecta is not associated with specific collagen mutations.** *Calcif Tissue Int*, 82 (4) (2008), pp. 263-270

[14] G.S. Barsh, K.E. David, P.H. Byers. **Type I osteogenesis imperfecta: a nonfunctional allele for pro alpha 1 (I) chains of type I procollagen.** *Proc Natl Acad Sci U S A*, 79 (12) (1982), pp. 3838-3842

[15] B. Sykes, M.J. Francis, R. Smith. **Altered relation of two collagen types in osteogenesis imperfecta.** *N Engl J Med*, 296 (21) (1977), pp. 1200-1203

[16] M.C. Willing, *et al.* **Osteogenesis imperfecta type I: molecular heterogeneity for COL1A1 null alleles of type I collagen.** *Am J Hum Genet*, 55 (4) (1994), pp. 638-647

[17] R.J. Wenstrup, *et al.* **Distinct biochemical phenotypes predict clinical severity in nonlethal variants of osteogenesis imperfecta.** *Am J Hum Genet*, 46 (5) (1990), pp. 975-982

[18] P.H. Byers, G.A. Wallis, M.C. Willing. **Osteogenesis imperfecta: translation of mutation to phenotype.** *J Med Genet*, 28 (7) (1991), pp. 433-442

[19] J.R. Shapiro. **Clinical and genetic classification of osteogenesis imperfecta and epidemiology.** J.R. Shapiro, *et al.* (Eds.), Osteogenesis imperfecta—a translational approach to brittle bone disease, Academic Press, San Diego, CA (2014), pp. 15-22

[20] J.P. Cassella, S.Y. Ali. **Abnormal collagen and mineral formation in osteogenesis imperfecta.** *Bone Miner*, 17 (2) (1992), pp. 123-128

[21] J.P. Cassella, *et al.* **A morphometric analysis of osteoid collagen fibril diameter in osteogenesis imperfecta.** *Bone*, 15 (3) (1994), pp. 329-334

[22] H. Stoss, P. Freisinger. **Collagen fibrils of osteoid in osteogenesis imperfecta: morphometrical analysis of the fibril diameter.** *Am J Med Genet*, 45 (1993), p. 257

[23] U. Vetter, *et al.* **Changes in apatite crystal size in bones of patients with osteogenesis imperfecta.** *Calcif Tissue Int*, 49 (4) (1991), pp. 248-250

[24] W. Traub, *et al.* **Ultrastructural studies of bones from patients with osteogenesis imperfecta.** *Matrix Biol*, 14 (4) (1994), pp. 337-345

[25] M. Weber, *et al.* **Pamidronate does not adversely affect bone intrinsic material properties in children with osteogenesis imperfecta.** *Bone*, 39 (3) (2006), pp. 616-622

[26] A. Boyde, *et al.*. **The mineralization density of iliac crest bone from children with osteogenesis imperfecta.** *Calcif Tissue Int*, 64 (3) (1999), pp. 185-190

[27] B.M. Misof, *et al.* **Differential effects of alendronate treatment on bone from growing osteogenesis imperfecta and wild-type mouse.** *Bone*, 36 (1) (2005), pp. 150-158

[28] S.H. Rao, *et al.* **Bisphosphonate treatment in the oim mouse model alters bone modeling during growth.** *J Biomech*, 41 (16) (2008), pp. 3371-3376

[29] K.J. Jepsen, *et al.* **Type I collagen mutation alters the strength and fatigue behavior of Mov13 cortical tissue.** *J Biomech*, 30 (11–12) (1997), pp. 1141-1147

[30] C. Albert, J. Jameson, G. Harris. **Design and validation of bending test method for characterization of miniature pediatric cortical bone specimens.** *Proc Inst Mech Eng H*, 227 (2) (2013), pp. 105-113

[31] C. Albert, *et al.* **Bone properties by nanoindentation in mild and severe osteogenesis imperfecta.** *Clin Biomech (Bristol, Avon)*, 28 (1) (2013), pp. 110-116

[32] Z. Fan, *et al.* **Mechanical properties of OI type III bone tissue measured by nanoindentation.** *J Biomed Mater Res A*, 79 (1) (2006), pp. 71-77

[33] Z. Fan, *et al.* **Comparison of nanoindentation measurements between osteogenesis imperfecta Type III and Type IV and between different anatomic locations (femur/tibia versus iliac crest).** *Connect Tissue Res*, 48 (2) (2007), pp. 70-75

[34] Z. Fan, *et al.* **Nanoindentation as a means for distinguishing clinical type of osteogenesis imperfecta.** *Compos B Eng*, 38 (3) (2007), pp. 411-415

[35] Z. Fan, *et al.* **Anisotropic properties of human tibial cortical bone as measured by nanoindentation.** *J Orthop Res*, 20 (4) (2002), pp. 806-810

[36] J.Y. Rho, *et al.* **Elastic properties of microstructural components of human bone tissue as measured by nanoindentation.** *J Biomed Mater Res*, 45 (1) (1999), pp. 48-54

[37] C.H. Turner, *et al.* **The elastic properties of trabecular and cortical bone tissues are similar: results from two microscopic measurement techniques.** *J Biomech*, 32 (4) (1999), pp. 437-441

[38] J.D. Currey. **The effects of strain rate, reconstruction and mineral content on some mechanical properties of bovine bone.** *J Biomech*, 8 (1) (1975), pp. 81-86

[39] J. Jameson, *et al.* **3D micron-scale imaging of the cortical bone canal network in human osteogenesis imperfecta (OI).** J.B. Weaver, R.C. Molthen (Eds.), Proceedings of SPIE, Medical Imaging 2013: Biomedical Applications in Molecular, Structural, and Functional Imaging, International Society for Optics and Photonics, Lake Buena Vista, FL (2013)

[40] U.E. Pazzaglia, *et al.* **The long bone deformity of osteogenesis imperfecta III: analysis of structural changes carried out with scanning electron microscopic morphometry.** *Calcif Tissue Int*, 93 (5) (2013), pp. 453-461

[41] ASTM-D790-07. **Standard methods for flexural properties of unreinforced and reinforced plastics and electrical insulating materials.** ASTM International, West Conschohocken, PA, USA (2006)

[42] A.A. MacDowell, *et al.* **X-ray micro-tomography at the Advanced Light Source.** SPIE 8506: Developments in X-ray Tomography VIII, International Society for Optics and Photonics, San Diego, CA (2012)

[43] A. Carriero, *et al.* **Altered lacunar and vascular porosity in osteogenesis imperfecta mouse bone as revealed by synchrotron tomography contributes to bone fragility.** *Bone*, 61 (2014), pp. 116-124

[44] P. Dong, *et al.* **3D osteocyte lacunar morphometric properties and distributions in human femoral cortical bone using synchrotron radiation micro-CT images.** *Bone*, 60 (2014), pp. 172-185

[45] C.A. Schneider, W.S. Rasband, K.W. Eiliceiri. **NIH image to ImageJ: 25 years of image analysis.** *Nat Methods*, 9 (7) (2012), pp. 671-675

[46] M. Doube, *et al.* **BoneJ: free and extensible bone image analysis in ImageJ.** *Bone*, 47 (6) (2010), pp. 1076-1079

[47] L. Cardoso, *et al.* **Advances in assessment of bone porosity, permeability and interstitial fluid flow.** *J Biomech*, 46 (2) (2013), pp. 253-265

[48] B.R. McCreadie, *et al.* **Osteocyte lacuna size and shape in women with and without osteoporotic fracture.** *J Biomech*, 37 (4) (2004), pp. 563-572

[49] Y. Carter, *et al.* **Variation in osteocyte lacunar morphology and density in the human femur–a synchrotron radiation micro-CT study.** *Bone*, 52 (1) (2013), pp. 126-132

[50] Y. Carter, *et al.* **Femoral osteocyte lacunar density, volume and morphology in women across the lifespan.** *J Struct Biol*, 183 (3) (2013), pp. 519-526

[51] A. Odgaard, H.J. Gundersen. **Quantification of connectivity in cancellous bone, with special emphasis on 3-D reconstructions.** *Bone*, 14 (2) (1993), pp. 173-182

[52] J. Toriwaki, T. Yonekura. **Euler number and connectivity indexes of a three-dimensional digital picture.** *Forma*, 17 (2002), pp. 183-209

[53] P. Tafforeau, *et al.* **Nature of laminations and mineralization in rhinoceros enamel using histology and X-ray synchrotron microtomography: potential implications for palaeoenvironmental isotopic studies.** *Palaeogeogr Palaeoclimatol Palaeoecol*, 246 (2007), pp. 206-227

[54] T.W. Ridler, S. Calvard. **Picture thresholding using an interative selection method.** *IEEE Trans Syst Man Cybern*, 8 (1978), pp. 630-632

[55] J.H. Hubbell. **Photon mass attenuation and energy-absorption coefficients from 1 keV to 20 MeV.** *Int J Appl Radiat Isot*, 33 (1982), pp. 1269-1290

[56] J.A. Bearden, A.F. Burr. **Reevaluation of X-ray atomic energy levels.** *Rev Mod Phys*, 39 (1967), pp. 125-142

[57] J.D. Currey. **The effect of porosity and mineral content on the Young's modulus of elasticity of compact bone.** *J Biomech*, 21 (2) (1988), pp. 131-139

[58] D.R. Carter, W.C. Hayes. **The compressive behavior of bone as a two-phase porous structure.** *J Bone Joint Surg Am*, 59 (7) (1977), pp. 954-962

[59] W.C. Hayes, S.J. Piazza, P.K. Zysset. **Biomechanics of fracture risk prediction of the hip and spine by quantitative computed tomography.** *Radiol Clin North Am*, 29 (1) (1991), pp. 1-18

[60] R.W. Goulet, *et al.* **The relationship between the structural and orthogonal compressive properties of trabecular bone.** *J Biomech*, 27 (4) (1994), pp. 375-389

[61] R. Hodgskinson, J.D. Currey. **Young's modulus, density and material properties in cancellous bone over a large density range.** *J Mater Sci Mater Med*, 3 (5) (1992), pp. 377-381

[62] D.R. Carter, W.C. Hayes. **Bone compressive strength: the influence of density and strain rate.** *Science*, 194 (4270) (1976), pp. 1174-1176

[63] S. Hengsberger, A. Kulik, P. Zysset. **Nanoindentation discriminates the elastic properties of individual human bone lamellae under dry and physiological conditions.** *Bone*, 30 (1) (2002), pp. 178-184
[64] C.E. Hoffler, *et al.* **An application of nanoindentation technique to measure bone tissue lamellae properties.** *J Biomech Eng*, 127 (7) (2005), pp. 1046-1053
[65] J.Y. Rho, G.M. Pharr. **Effects of drying on the mechanical properties of bovine femur measured by nanoindentation.** *J Mater Sci Mater Med*, 10 (8) (1999), pp. 485-488
[66] C. Hirsch, F.G. Evans. **Studies on some physical properties of infant compact bone.** *Acta Orthop Scand*, 35 (1965), pp. 300-303
[67] J. Currey. **What determines the bending strength of compact bone?.** *J Exp Biol*, 202 (1999), pp. 2495-2503
[68] J.D. Currey, G. Butler. **The mechanical properties of bone tissue in children.** *J Bone Joint Surg Am*, 57 (6) (1975), pp. 810-814
[69] K. Choi, S.A. Goldstein. **A comparison of the fatigue behavior of human trabecular and cortical bone tissue.** *J Biomech*, 25 (12) (1992), pp. 1371-1381
[70] K. Choi, *et al.* **The elastic moduli of human subchondral, trabecular, and cortical bone tissue and the size-dependency of cortical bone modulus.** *J Biomech*, 23 (11) (1990), pp. 1103-1113
[71] E.R. Draper, A.E. Goodship. **A novel technique for four-point bending of small bone samples with semi-automatic analysis.** *J Biomech*, 36 (10) (2003), pp. 1497-1502
[72] J.P. Berteau, *et al.* **In vitro ultrasonic and mechanic characterization of the modulus of elasticity of children cortical bone.** *Ultrasonics*, 54 (5) (2014), pp. 1270-1276
[73] A.H. Burstein, *et al.* **The ultimate properties of bone tissue: the effects of yielding.** *J Biomech*, 5 (1) (1972), pp. 35-44
[74] J. Currey. **Bones: structure and mechanics.** (2nd Edition), Princeton University Press, Princeton NJ (2002)
[75] ASTM-C674-88. **Standard test methods for flexural properteis of ceramic whiteware materials.** ASTM International, West Conshohocken, PA, USA (2006)
[76] H.C. Spatz, E.J. O'Leary, J.F. Vincent. **Young's moduli and shear moduli in cortical bone.** *Proc Biol Sci*, 263 (1368) (1996), pp. 287-294
[77] S.A. Feik, C.D.L. Thomas, J.G. Clement. **Age-related changes in cortical porosity of the midshaft of the human femur.** *J Anat*, 191 (1997), pp. 407-416
[78] V. Bousson, *et al.* **CT of the middiaphyseal femur: cortical bone mineral density and relation to porosity.** *Radiology*, 217 (1) (2000), pp. 179-187
[79] M.D. Landrigan, *et al.* **Contrast-enhanced micro-computed tomography of fatigue microdamage accumulation in human cortical bone.** *Bone*, 48 (3) (2011), pp. 443-450
[80] F.J. O'Brien, *et al.* **Visualisation of three-dimensional microcracks in compact bone.** *J Anat*, 197 (Pt 3) (2000), pp. 413-420
[81] S. Mohsin, F.J. O'Brien, T.C. Lee. **Microcracks in compact bone: a three-dimensional view.** *J Anat*, 209 (1) (2006), pp. 119-124
[82] R. Voide, *et al.* **Time-lapsed assessment of microcrack initiation and propagation in murine cortical bone at submicrometer resolution.** *Bone*, 45 (2) (2009), pp. 164-173
[83] H. Leng, *et al.* **Micro-computed tomography of fatigue microdamage in cortical bone using a barium sulfate contrast agent.** *J Mech Behav Biomed Mater*, 1 (1) (2008), pp. 68-75
[84] H.D. Barth, *et al.* **On the effect of X-ray irradiation on the deformation and fracture behavior of human cortical bone.** *Bone*, 46 (6) (2010), pp. 1475-1485
[85] X.N. Dong, X.E. Guo. **The dependence of transversely isotropic elasticity of human femoral cortical bone on porosity.** *J Biomech*, 37 (8) (2004), pp. 1281-1287
[86] J. Currey. **Stress concentrations in bone.** *Q J Microsc Sci*, 103 (1962), pp. 111-133
[87] R. Hodgskinson, *et al.* **The ability of ultrasound velocity to predict the stiffness of cancellous bone in vitro.** *Bone*, 21 (2) (1997), pp. 183-190

[88] J.C. Lotz, T.N. Gerhart, W.C. Hayes. **Mechanical properties of metaphyseal bone in the proximal femur.** *J Biomech*, 24 (5) (1991), pp. 317-329
[89] B.R. McCreadie, S.J. Hollister. **Strain concentrations surrounding an ellipsoid model of lacunae and osteocytes.** *Comput Methods Biomech Biomed Engin*, 1 (1) (1997), pp. 61-68
[90] D. Nicollela, *et al.* **Osteocyte lacunae tissue strain in cortical bone.** *J Biomech*, 39 (9) (2006), p. 1745-1743
[91] G.C. Reilly. **Observations of microdamage around osteocyte lacunae in bone.** *J Biomech*, 33 (9) (2000), pp. 1131-1134
[92] P.E. Palacio-Mancheno, *et al.* **3D assessment of cortical bone porosity and tissue mineral density using high-resolution microCT: effects of resolution and threshold method.** *J Bone Miner Res*, 29 (1) (2014), pp. 142-150
[93] D. Vashishth, *et al.* **Determination of bone volume by osteocyte population.** *Anat Rec*, 267 (4) (2002), pp. 292-295
[94] D. Vashishth, *et al.* **Decline in osteocyte lacunar density in human cortical bone is associated with accumulation of microcracks with age.** *Bone*, 26 (4) (2000), pp. 375-380
[95] K.M. Hannah, *et al.* **Bimodal distribution of osteocyte lacunar size in the human femoral cortex as revealed by micro-CT.** *Bone*, 47 (5) (2010), pp. 866-871
[96] M.G. Mullender, *et al.* **Differences in osteocyte density and bone histomorphometry between men and women and between healthy and osteoporotic subjects.** *Calcif Tissue Int*, 77 (5) (2005), pp. 291-296
[97] T. Bellido, L.I. Plotkin. **Novel actions of bisphosphonates in bone: preservation of osteoblast and osteocyte viability.** *Bone*, 49 (1) (2011), pp. 50-55
[98] H. Plotkin, *et al.* **Pamidronate treatment of severe osteogenesis imperfecta in children under 3 years of age.** *J Clin Endocrinol Metab*, 85 (5) (2000), pp. 1846-1850
[99] F.H. Glorieux, *et al.* **Cyclic administration of pamidronate in children with severe osteogenesis imperfecta.** *N Engl J Med*, 339 (14) (1998), pp. 947-952
[100] U.A. Liberman, *et al.* **Effect of oral alendronate on bone mineral density and the incidence of fractures in postmenopausal osteoporosis. The Alendronate Phase III Osteoporosis Treatment Study Group.** *N Engl J Med*, 333 (22) (1995), pp. 1437-1443
[101] D.M. Black, *et al.* **Randomised trial of effect of alendronate on risk of fracture in women with existing vertebral fractures. Fracture Intervention Trial Research Group.** *Lancet*, 348 (9041) (1996), pp. 1535-1541
[102] F. Rauch, F.H. Glorieux. **Osteogenesis imperfecta.** *Lancet*, 363 (9418) (2004), pp. 1377-1385
[103] F. Rauch. **Bisphosphonate treatment and related agents in children.** J.R. Shapiro, *et al.* (Eds.), Osteogenesis imperfecta - a translational approach to brittle bone disease, Academic Press, San Diego, CA (2014), pp. 501-507
[104] J.C. Marini. **Bone: use of bisphosphonates in children—proceed with caution.** *Nat Rev Endocrinol*, 5 (5) (2009), pp. 241-243
[105] T.E. Uveges, *et al.* **Alendronate treatment of the Brtl osteogenesis imperfecta mouse improves femoral geometry and load response before fracture but decreases predicted material properties and has detrimental effects on osteoblasts and bone formation.** *J Bone Miner Res*, 24 (5) (2009), pp. 849-859
[106] R.C. Guerri-Fernandez, *et al.* **Microindentation for in vivo measurement of bone tissue material properties in atypical femoral fracture patients and controls.** *J Bone Miner Res*, 28 (1) (2013), pp. 162-168
[107] Y. Yamagami, *et al.* **Effects of minodronic acid and alendronate on bone remodeling, microdamage accumulation, degree of mineralization and bone mechanical properties in ovariectomized cynomolgus monkeys.** *Bone*, 54 (1) (2013), pp. 1-7
[108] L. Hyldstrup, *et al.* **Response of cortical bone to antiresorptive treatment.** *Calcif Tissue Int*, 68 (3) (2001), pp. 135-139

[109] B. Borah, *et al.* **Risedronate reduces intracortical porosity in women with osteoporosis.** *J Bone Miner Res*, 25 (1) (2010), pp. 41-47

[110] J. Liu, *et al.* **Bisphosphonates and risk of subtrochanteric, femoral shaft, and atypical femur fracture: sensitivity and trim and fill studies.** *Genet Test Mol Biomarkers*, 18 (2) (2014), pp. 117-122

[111] V. Bottai, *et al.* **Atypical femoral fractures: retrospective radiological study of 319 femoral fractures and presentation of clinical cases.** *Osteoporos* Int, 25 (3) (2014), pp. 993-997